



Sodium effect on static mechanical behavior of MD-modeled sodium silicate glasses



Gergely Molnár^{a,*}, Patrick Ganster^a, János Török^b, Anne Tanguy^c

^a Ecole de Mines de Saint-Etienne, Centre SMS, Laboratoire Georges Friedel CNRS-UMR5307, 158 Cours Fauriel, 42023 Saint-Etienne, France

^b Department of Theoretical Physics, Budapest University of Technology and Economics, Budapest H-1111, Hungary

^c Université de Lyon, LaMCoS, INSA-Lyon, CNRS UMR5259, F-69621, France

ARTICLE INFO

Article history:

Received 20 November 2015

Received in revised form 25 February 2016

Accepted 26 February 2016

Available online xxxx

Keywords:

Multi-scale modeling

Micro-mechanics

Sodium silicate

Local elasticity

Molecular dynamics

ABSTRACT

The structural and elastic mechanical properties of $x\text{Na}_2\text{O}-(100-x)\text{SiO}_2$ sodium silicate glasses were computed and analyzed at different scales, using atomistic simulations and coarse-grain methods based on physical principles. The numerical simulations were performed on large samples ($\sim 100^3 \text{ \AA}^3$ box size with $\sim 70\,000$ atoms), and the results were compared to experimental measurements. It was shown that the cutoff in the non-Coulombic part of the empirical interactions affects the pressure/density relations. Therefore, this value was tuned to achieve the experimental density at ambient pressure. As a result we obtained realistic mechanical and structural properties as well. With this model, we analyzed the elastic response of the samples for different sodium content. We showed, that experimentally measured elastic moduli result from a succession of micro-plastic rearrangements that must be taken into account when calculating microscopic elastic moduli. Moreover, we investigated the size dependence of the elastic moduli, and we showed a strong connection between small scale heterogeneous elasticity and sodium repartition. The transition from small scale to large scale description of elasticity should involve an accurate description of the spatial organization of sodium ions inside the silica network.

© 2016 Elsevier B.V. All rights reserved.

1. Introduction

Understanding the relationship between mechanical and structural properties in silicate glasses is a challenging task. Indeed, silicate glasses are widely used in cements [1], in passive fire protection, and in the automotive sector [2]. Sodium silicate glasses are of huge interest to academia and industry as they are used as setting and hardening accelerators for cements [3]. However, diverse glass compositions break in different ways and for all these applications, it is important to deal with the composition dependence of the mechanical behavior. For example, soda-lime-silica, which is one of the most popular architectural materials nowadays [4], has a much more ductile behavior than pure silica, even if silica has a higher macroscopic strength [5]. Failure properties are very sensitive to local ductility [6]. Plastic behavior in amorphous systems was directly related to the local elastic heterogeneities [7]. But the connection between local structure and elastic properties is still a matter of debate in disordered materials. It is not clear for example whether specific species at different densities will give rise to stiffening or softening at a macroscopic level, and if it is possible to relate a structural defect (like a coordination defect) to local softening. Indeed, the microscopic basis of the apparent linear elastic behavior at a macroscopic scale in glasses is even not clearly established, due to

the spatial heterogeneities, and to the large distribution of energy barriers in these metastable materials [8].

In this study, we concentrate on the structural and elastic properties of sodium silicate glasses that are an intermediate composition between soda-lime-silica and silica as they contain only one network modifier. One requirement is to identify the role of additional species on the structural and elastic properties of the glass, and to estimate the smallest scale where the material can be described accurately enough by a spatially constant constitutive model. This scale corresponds to the size of the representative volume element [9–11] (RVE), which is crucial to develop continuum models later. For this endeavor, we performed atomic simulations using classical molecular dynamics scheme (MD) which is employed by many authors to analyze the structural [12–23] and mechanical [24–30] properties of silica and sodium silicate. Several studies [13,16,17] compared successfully the static and dynamic structural properties of modeled sodium silicate with experimental results. Nevertheless, the mechanical behavior remains much less studied and mainly for very small system sizes [31,32]. However, the identification of the RVE [33–35] is essential to transfer the atomistic results to larger scales. Therefore, it is important to check that the results are independent of the size of the simulation box. The identification of the RVE can then be made only if a scale exists, above which the mechanical parameters do not vary anymore. In this paper, we will focus on the elastic response, and we will give atomistic foundation of the elastic moduli computed at different scales. Among other questions,

* Corresponding author.

E-mail address: gmlnarn.work@gmail.com (G. Molnár).

the connection between effective elastic moduli measured at large scale and local mechanical reversibility will be discussed, as well as the convergence from an elastic heterogeneous behavior to a homogeneous behavior at large scale. Indeed, it is now well established that disorder induces meso-scale rotational correlations [33,36] with a size comparable to the scale above, which the system becomes isotropic and homogeneous [7]. The role of the microstructure on this effect is still a matter of debate [37] as well as the role of the precision in the measurement of the elastic moduli [8,30], in connection with possible irreversible small-scale processes. In this paper the results of atomistic simulations are analyzed using coarse-graining technique to describe the mechanical response at different scales and with different degrees of precision. Sufficiently large samples ($\approx 100^3 \text{ \AA}^3$) were used to reduce the effect of periodic boundaries [38] and finite size effects are discussed. After delineating the method and validating the structures of our models via experimental data of neutron scattering [39–42] and local connectivity (mainly NMR) analysis [43–46] we concentrate on the apparent elastic mechanical behavior at different scales, and on its chemical sensitivity. The results give not only insights into the microscopic origin of the elastic heterogeneities, but could also be used in continuum based models and simulations [47–49].

The paper is organized as follows: in Section 2, we introduce the basic numerical techniques used. The importance of the potential function is outlined. How and why this numerical parameter can change significantly the mechanical results of the simulations is brought up. The verification of the models was done with the detailed structural analysis compared to experimental results. In Section 3 the macroscopic results of a quasi-static deformation is shown. The mechanical parameters are derived using both global and local methods. Plus, local mechanical properties, i.e. stiffer and softer regions are related to structural ones, highlighting the effect of sodium distribution in disordered silica network and heterogeneous elasticity. Finally a general discussion and the conclusion are presented.

2. General description of the system

In this part, we describe the simulations with a special care devoted to the pressure/density relationship. Comparison of the structural properties to experimental data is presented.

2.1. Atomic system generation

The amorphous glass samples were generated by random sequential placement of the atoms in a periodic simulation box after which molecular dynamics simulations using LAMMPS software [50] were used to equilibrate, quench and test the samples. Classical molecular dynamics (MD) simulation is a numerical scheme to solve the classical Newton's equation of motion for a system of N atoms interacting via empirical potentials, detailed later, and with different external inputs (like a constant temperature and pressure – NPT ensemble). The $x\text{Na}_2\text{O}-(100-x)\text{SiO}_2$ glass models with $x = 5, 10, 15, 20, 30$ and 40%mol were generated following the method explained below, with $\sim 70\,000$ atoms in a box of final length of $\sim 100 \text{ \AA}$, as detailed in Table 1. Other system sizes ($L = 10 \text{ \AA}, L = 20 \text{ \AA}, L = 30 \text{ \AA}, L = 50 \text{ \AA}$ and $L = 150 \text{ \AA}$ with respectively 75, 600, 2000, 9000 and 250 000 atoms) were also studied at the same pressure, in order to test finite size effects.

Table 1

Detailed system information: nominal composition (x_{nom}), precise composition (x_{prec}), number of atoms (N), final simulation box size (L_0) and density (ρ_0) at zero pressure.

x_{nom} [%mol]	5	10	15	20	30	40
x_{prec} [%mol]	4.998	9.998	14.99	19.99	30.00	40.00
N [–]	67 041	68 472	69 849	70 926	73 368	74 604
L_0 [Å]	99.71	99.76	99.92	99.84	99.86	99.89
ρ_0 [g/cm ³]	2.25	2.30	2.34	2.38	2.47	2.52

The atoms were placed randomly, taking care that the minimum distance is larger than 1.5 \AA . Using NPT ensemble simulations with Berendsen barostat [51] and Nosé–Hoover thermostat [52], the systems were first equilibrated at the liquid state of 3000 K and zero pressure ($\pm 5 \text{ MPa}$) for 1.4 ps with a coupling time of one timestep (1 fs) to the thermostat. This way the initial explosion of the kinetic energy was controlled without particle collisions. After this short period the coupling time to the thermostat was set to 2 ps. The systems were then melted for 100 ps at 3000 K. We did not increase further the initial melting temperature because at higher temperature ranges the repulsive part of the potential function becomes active which dilutes the results [12]. Then the liquids were quenched with the cooling rate of 10 K/ps (10^{+13} K/s) down to a final total kinetic energy ($E_{kin} \sim 10^{-4} \text{ eV}$) which corresponded to 10^{-5} K temperature. Finally the systems were equilibrated for 100 ps and the total energy of the systems was minimized using Polak–Ribiere conjugate gradient algorithm to reach static equilibrium. This quenching rate may seem fast, although it was shown in Ref. [12,53,54] and also double checked by this study that neither structural nor density properties change furthermore by decreasing this parameter [55].

2.2. Potential function

From several types of empirical potential functions developed to describe sodium silicate glasses [56,57,31,58], we chose to adapt the so-called van Beest, Kramer and van Santen (BKS) potential [57] which was extensively studied. We used the parameters set according to the work of Yuan and Cormack [16]. The two-body potential function used in this paper can be described as follows:

$$\Phi_{\alpha\beta}^{\text{BKS}}(r) = \begin{cases} \Phi_{\alpha\beta}^{\text{Coul}}(r) + \Phi_{\alpha\beta}^{\text{Buck}}(r)G(r, r_{cut}, \gamma) & \text{for } r \geq r_{rep}, \\ \Phi_{\alpha\beta}^{\text{Coul}}(r) + \Phi_{\alpha\beta}^{\text{Rep}}(r) & \text{for } r < r_{rep}, \end{cases} \quad (1)$$

where

$$\Phi_{\alpha\beta}^{\text{Buck}}(r) = A_{\alpha\beta} e^{-r/\rho_{\alpha\beta}} - C_{\alpha\beta}/r^6, \quad (2)$$

$$G(r, r_{cut}, \gamma) = e^{-\gamma^2/(r_{cut}-r)^2}, \quad (3)$$

$$\Phi_{\alpha\beta}^{\text{Rep}}(r) = D_{\alpha\beta}/r^{12} + rE_{\alpha\beta} + F_{\alpha\beta}. \quad (4)$$

In Eq. (1), α and β correspond to the different species (Si, O or Na) and r is the distance between two atoms. $\Phi_{\alpha\beta}^{\text{Buck}}$ is the well known Buckingham term, which was set according to the parameters ($A_{\alpha\beta}, \rho_{\alpha\beta}, C_{\alpha\beta}$) of Yuan and Cormack [16].

In addition to this description, the $G(r, r_{cut}, \gamma=0.5)$ cutoff function was added to the Buckingham potential to ensure that the potential energy and its first derivative (contact force) goes smoothly to zero at the distance equal to the cutoff (r_{cut}). A stronger very short range (if $r < r_{rep}$) repulsive potential (see in Eq. (4)) was added to the traditional BKS potential in order to avoid the collapse of atoms at high pressure or temperature as usually seen [59–61,30]. $D_{\alpha\beta}, E_{\alpha\beta}$, and $F_{\alpha\beta}$ have been set, that the potential function and its first and second derivative stays continuous. r_{rep} was taken as close as possible to r_0 (distance, where the potential function has its maximum) in order to have a repulsive effect at small r values. The classic Coulomb interactions in Eq. (2) ($\Phi_{\alpha\beta}^{\text{Coul}} = k \frac{q_\alpha q_\beta}{r}$, where k is Coulomb's constant) are calculated using partial charges ($q_0 = -1.2, q_{Si} = +2.4$ and $q_{Na} = +0.6$) [16]. To take periodic boundaries into account a long term PPPM solver was applied with the maximum of 10^{-4} relative root mean square error in forces. This standard potential was already used to study the structural and some mechanical properties of sodium-silicate samples. Our work studies extensively the related mechanical response at different scales,

and the role of the cutoff parameter r_{cut} . We have compared some of the results as well to those given with the potential of Pedone et al. [31] which involves a different expression for the Buckingham function.

It needs to be emphasized that our work is not meant to propose a new potential function. It is about to show how the cutoff value can fine-tune the BKS potential to achieve the experimental density values with adequate stiffness constants. Without this modification neither would be sufficient to reproduce macroscopic mechanical properties.

It is well known that the cutoff value r_{cut} has an effect on the calculated pressure [12,62–64], however there are different ways to introduce a cutoff in the empirical interactions. In this paper, the cutoff is acting only on the non-Coulombic part of the interactions. The Coulombic part of the interactions is kept in their original form in order to preserve charge neutrality. The cutoff applies only on the shorter range interactions. Generally, a cutoff is used to reduce the computational demand. The truncation of the interatomic potential at a cutoff introduces some difficulties in defining a consistent potential and force for use in molecular dynamics. By applying this method, a relatively small jump appears in both the potential, and the force function at the cutoff. When calculating global energies and pressure, this artifact causes huge fluctuations due to this discontinuity. This can be avoided by applying some kind of correction function [65]. The simplest case is, if a constant value is subtracted from the potential. However, this does not solve the problem of the forces. The second step would be to subtract a linear function from the potential, thus a constant value from the force. In practice [16] more advanced, differentiable functions [66] are used, as well as in our case (Eq. (3)).

Using a unified value for the cutoff parameter, the BKS potential does not reproduce experimental densities and stiffness properties adequately. Therefore, an additional correction has to be applied. This could be a simple normalization of the density (for NPT) or an initial pressure correction (for NVT). Both methods artificially change the computed macroscopic mechanical properties, and do not decrease the difference between the stiffness constants measured and calculated. In this study the cutoff value was chosen to fine-tune the simulated density values, consequently achieving good pressure–density relationships and adequate stiffness properties as well. Unfortunately, we did not find a unified value for the cutoff parameter as function composition, therefore we propose to change r_{cut} with the added sodium-oxide.

The difference of the force and stiffness obtained with and without the cutoff value is shown in Fig. 1 for different cutoff values ($r_{cut} = 5, 9, 13 \text{ \AA}$) and Si–O pairs. The interactions depend of course on the cutoff value which affects the forces and consequently the calculated pressure and mechanical properties. There is a tendency that the use of a small cutoff implies an increase of the effective repulsive force at small distances (see Fig. 1) and thus, of the macroscopic pressure, due to the decay of the attractive van der Waals contribution.

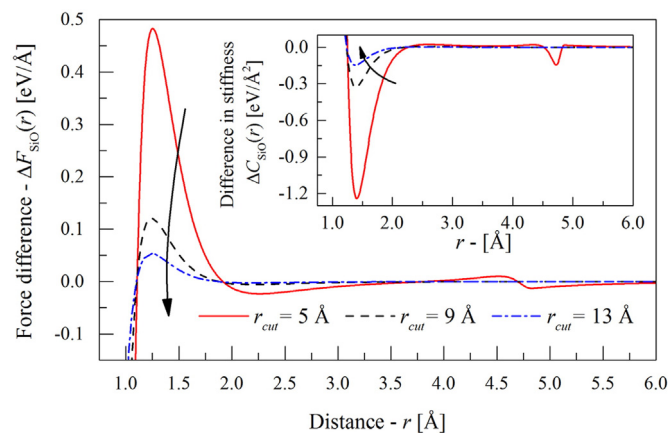


Fig. 1. The difference between contact forces with and without cutoff for the Buckingham potential of Si–O pairs (inset: same for stiffness). Cutoff values are $r_{cut} = 5, 9$ and 13 \AA .

One would naively think that the larger the cutoff the better it is, however it seems that to match the glass densities measured in actual experiments, a moderate value for the cutoff is needed. In addition, this choice also ensured that the final pressure remains low ($\pm 5 \text{ MPa}$).

Note that, this small composition dependence of the cutoff value raises interesting questions about the possible role of composition on the screening of short-range interactions. These interactions being considered as homogeneous beyond the cutoff distance. This could be related to mutual orientations of instantaneous dipolar interactions not described in the initial version of the BKS potential [67], and already evidenced for Coulombic interactions [68]. But this question is not the purpose of our paper: our main worry being to achieve good structural properties and pressure–density relations as well, thanks to an empirical adjustment of this simple parameter.

2.3. Density

In Fig. 2(a) both simulated (black triangles and crosses) and experimentally measured [69,70] density values are plotted for different sodium silicate compositions. Similarly, we found that the density increases as a non-linear function with the cutoff as shown in the inset of Fig. 2(b). As aforementioned, the interaction cutoff was chosen such that the observed density at $\pm 5 \text{ MPa}$ pressure matches the results of the most recent experiment [70]. It shows a linear increase with the sodium content (see Fig. 2(b)). The linear fit then allows for creating simulations of new compositions without the need of further calibration.

It has to be noted that applying the cutoff at a constant distance ($r_{cut} = 5.5 \text{ \AA}$) would not allow us to reproduce experimental density values. At $x = 10\%$ mol, the density is reproduced in an adequate way, but above this composition the simulations underestimate the materials density.

It was shown in the inset of Fig. 1 that the individual stiffness of the bonds rises by increasing the cutoff distance. The global stiffness of the full system is affected consequently. This effect is demonstrated in Fig. 3(a) where the Young's and bulk modulus are computed for 5% Na_2O –95% SiO_2 as explained later. An increase of 20% was found of the Young's modulus for a cutoff change of factor 2, underlining again the importance of the proper choice of the cutoff values. The effect of this parameter is far larger than the quenching rates varying over few magnitudes (see Fig. 3(b)).

2.4. Structural analysis

Visualization of structural inhomogeneities can be done by looking at the local density of sodium (Fig. 4). In order to test the often proposed hypothesis, that sodium is arranged along channel-like formations [17,

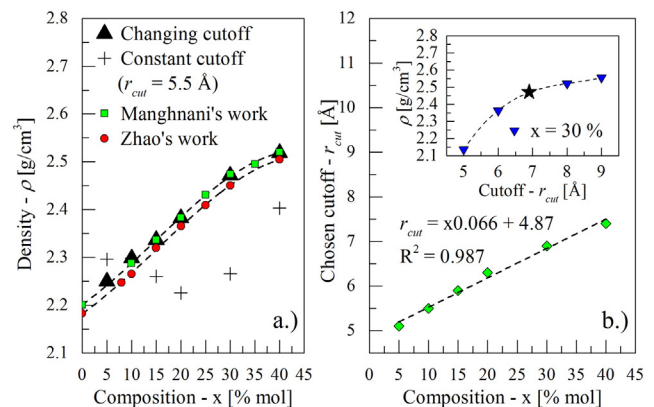


Fig. 2. a.) Simulated density (fine-tuned cutoff – black triangles; constant 5.5 \AA cutoff – crosses) compared with experimental value (Manghani's work [69], Zhao's work [70]). b.) Chosen cutoff for different compositions with linear fit (inset: density as a function of cutoff with 3rd order polynomial fit and the chosen cutoff indicated by the star).

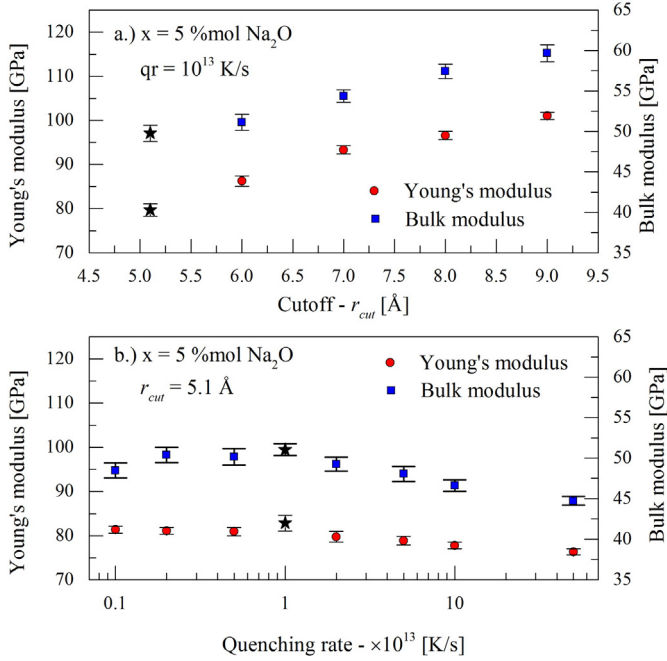


Fig. 3. Global Young's and bulk modulus as a function of the interaction cutoff (a.) and quenching rate (b.) for $x = 5\%$ mol Na_2O . Stars indicate the cutoff value and the quenching rate used in the detailed simulations.

[20,71–76], we drew different iso-density surfaces for different density values in Fig. 4. The following continuous coarse-grained expression was used for the density given by

$$\rho(\mathbf{r}) = \sum_i m_i \phi(\|\mathbf{r} - \mathbf{r}_i\|), \quad \text{and} \quad \phi(r) = \frac{1}{\pi^{3/2} w^3} e^{-(r/w)^2}, \quad (5)$$

where \mathbf{r}_i is the position of atom i with mass m_i , \mathbf{r} is the position of the observed grid point and w is the coarse-graining scale. It can be seen in Fig. 4 (with $w = 8 \text{ \AA}$), that high density regions are positioned on small isolated pockets, but for smaller atom densities one can see that these pockets grow into connected channel-like shapes. This confirms the hypothesis that sodium has a medium range order and that it is positioned among the silica structures. The sodium atoms do not penetrate isotropically the original silicon-oxygen network. This can be an additional reason for the deviation from the mean-field description.

This channel like feature is tested with a percolation analysis [77]. The regions with sodium density above ρ_l form isolated islands. These pockets transform into a percolating cluster at a critical density ($\rho_{l,c}$), which was found to be $\rho_{l,c} = 10.60 \text{ atom/nm}^3$. At this point the chosen region fills only 8.3% of the simulation box. This value is the third of what is required for the percolating cluster on a random 3D cubic lattice. This suggests that high density sodium regions have local correlations.

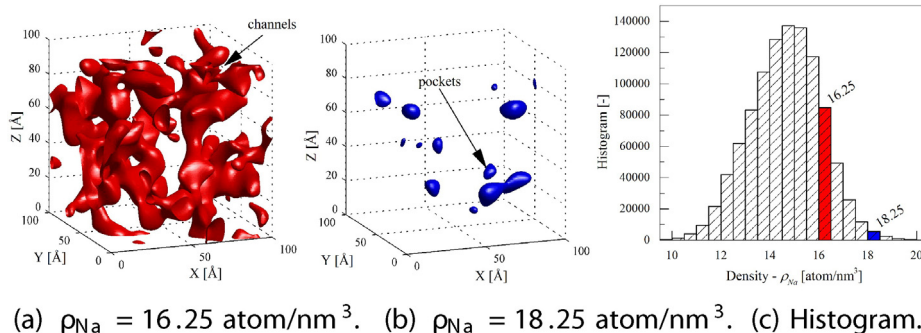


Fig. 4. Sodium density isosurfaces of sodium rich regions (mean value is: 14.65 atom/nm^3) for $x = 30\%$ mol Na_2O , with the coarse-graining scale of $w = 8 \text{ \AA}$.

Such a low percolation density can be obtained also by the random placement of prolate ellipsoids with the aspect ratio of 8 [78]. The percolation cluster created with prolate ellipsoids has a channel like structure similarly to the high density sodium regions in Fig. 4(a). We have tested this assumption by an ellipsoid insertion algorithm [79], where the largest possible ellipsoids was fitted into the given object. The analysis also showed the high occurrence of prolate ellipsoids with the aspect ratio of 7–9, confirming the percolation results. We can conclude from this analysis that the high density sodium regions form channel like structures with aspect ratio of 8.

In Fig. 5 experimental [41] neutron and X-ray (inset) structure factors are compared with the simulated ones using ISAACS [80] for 30% Na_2O –70% SiO_2 sodium silicate glass. Numerical comparison can be made using a χ^2 test: $\chi^2 = \sum_{i=1}^{n_p} (S(q_i)_{MD} - S(q_i)_{Experimental})^2 / n_p$, where $S(q_i)$ is the value of the function at q_i and n_p is the number of q_i points. The difference between the two functions are $\chi^2_{Neutron} = 2.6 \cdot 10^{-3}$ and $\chi^2_{X-ray} = 2.4 \cdot 10^{-3}$, which can be considered relatively low. Furthermore the peaks of the functions are in corresponding places.

A better interpretation of the scattering results can be made with the total correlation functions (TCF) calculated from the Fourier transform of the structure factors. The calculated TCF shown in Fig. 6 displays a very good match with the experimental data of Fábíán et al. [41]. Good correspondence was also observed while comparing partial pair distribution functions as it is shown in Fig. 7. We found a discrepancy between Na–Na pairs. However, the peak position of this function in the literature is highly dependent on the small distance hard sphere cutoff (2.5 \AA for Ref. [41]) used in reverse Monte-Carlo simulation performed to transform experimental data [39–41]. For example in Ref. [39] the authors set this parameter to 3.1 \AA and the peak was found at 3.2 \AA . Thus, it is not a reliably comparable parameter. This fact was checked by the authors of present paper as well.

To compare two structures, another standard measurement is the connectivity of the silica system (Q^n distribution). Therefore, we focused on the number of bridging (BO) and non-bridging oxygen (NBO) atoms around a silicon to describe the connectivity of the silica system. This number was calculated by counting BO atoms, whose position to the central silicon atom was closer than 1.7 \AA . This distance is the first local minimum (1.7 \AA) after the first peak (1.6 \AA) of the corresponding Si–O pair distribution function. We considered bridging oxygens if they had two silicon atoms at a distance closer than 1.7 \AA . All other oxygens were considered NBOs. The Q^n species ($n = 4, 3, 2, 1, 0$) are defined as Si atoms having n BO atoms. Table 2 shows comparison between the Q^n distribution obtained by our simulation and NMR measurements [43–45]. 20% Na_2O content was chosen because this is the composition for which the most experimental measurements exists in literature. Our results lie within the scatter of the experimental results.

In Table 3 the distributions of different Q^n species are shown as function of composition. The increment of the sodium content decreases the amount of Q^4 tetrahedral silicons, and increases the amount of less

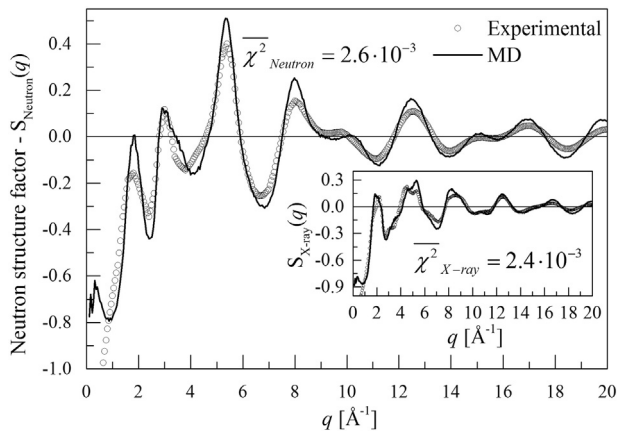


Fig. 5. Comparison between neutron and X-ray structure factor obtained by experiments [41] (circles) and MD simulation (black line) for $x = 30\%$ mol Na_2O .

perfect formations (Q^0, Q^1, Q^2, Q^3). Also in Table 3 we can see the change of the bridging (BO) and non-bridging oxygens (NBO) ratio. As expected, by the adding Na the number of non bridging oxygens increases, with the decay of the amount of Q^4 silicons. From these observations it is obvious, that sodium acts as network modifier which alters the atomic structure. It is usually present as ion, compensated by non-bridging oxygen atoms. NBOs are bonded by one covalent bond to the original silica network and holding a negative charge to compensate for the positive sodium ion nearby. The presence of non-bridging oxygens lowers the relative number of strong bonds in the material and this way weakens the network.

We have shown in this part, that the comparison between the simulation and experimental data is adequate, and is within the accuracy of the most recent experimental measurements. In summary the network of the simulated material is in agreement with the experimentally measured sodium silicate structure, with channel-like organization of sodium along percolating clusters that have been adequately characterized. We will now look at the related mechanical properties.

3. Mechanical results

The following section focuses on the analysis of the macroscopic and microscopic elastic properties for different compositions. For that purpose, a detailed coarse-grain analysis was performed by looking first at the effect of cumulative applied strain, and then at the spatial distribution of the elastic moduli.

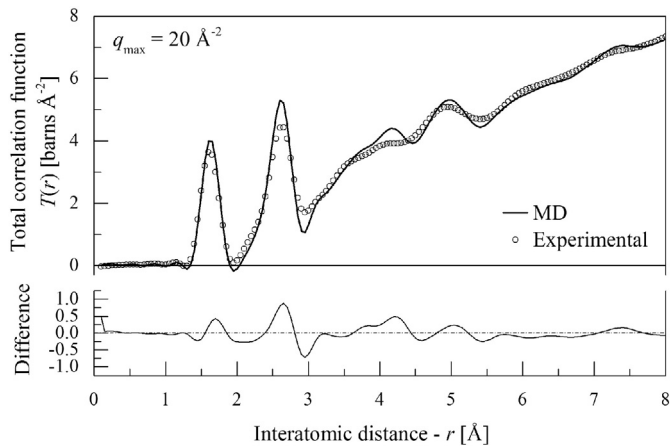


Fig. 6. Top: Total correlation functions calculated from neutron scattering [41] and MD simulation. Bottom: Difference between MD simulations and experimental measurements from for $x = 30\%$ mol Na_2O .

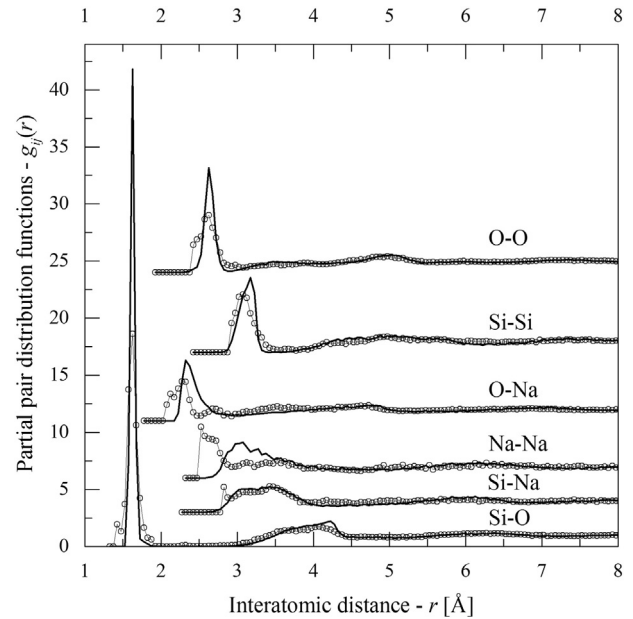


Fig. 7. Partial pair distribution functions obtained by different methods for $x = 30\%$ mol Na_2O : MD (black line), Experimental + RMC [41] (circles).

3.1. System deformation

After minimizing both kinetic and potential energy every sample was tested to evaluate its elastic mechanical properties. We focused on the quasi-static athermal limit, where thermal effects and related viscous processes are assumed to be negligible in comparison with elastic and plastic properties. This assumption is reasonable for glasses below the glass transition temperature [37]. When the mechanical load is slow, the static method is more preferred than the dynamic method. The static method [81] corresponds to a number of successive deformation steps followed by a minimization in order to map local minima on the potential energy hypersurface. The dynamic method [51,82] involves the solution of the equation of motion as a constant stress molecular dynamics simulation. This way, the shape of the simulation box is changed in order to achieve a desired stress state. The dynamics method was used during the creation of the system that is a short time high-temperature process. For quasi-static (low frequency) mechanical load, it is more convenient to use the static method. The static method is also more suitable than any statistical physics inspired method [83], due to the lack of thermodynamical equilibrium in the glassy state. Upon mechanical load, the system evolves from one metastable state to another. The only assumption made in the athermal limit is that below the glass transition temperature, thermal activity is negligible in comparison with mechanically driven one. This method allows finally a clear identification of reversible and irreversible steps, as will be discussed later.

The deformation is imposed on the periodic simulation box in a homogeneous way and the system is then relaxed in order to reach an

Table 2

Q^n species in sodium silicate containing $x = 20\%$ mol Na_2O with the theoretical bond length $r_{\text{Si-O}} = 1.7 \text{ \AA}$. Experimental data were taken from Emerson [43], Maekawa [44] and Charpentier [45] (with two different methods).

Q^n	This work	Emerson	Maekawa	Charpentier
Q^0	0.04%	0%	0%	0%
Q^1	0.82%	0%	0%	0%
Q^2	8.42%	6%	2%	8.33%
Q^3	38.81%	40%	48%	33.33%
Q^4	51.91%	54%	50%	58.34%

Table 3
Qⁿ species and BO–NBO ratio for different simulated composition.

NaO [%mol]	Q ⁰ [%]	Q ¹	Q ²	Q ³	Q ⁴	BO	NBO
%	0.02	0.25	1.02	13.72	84.97	93.39	6.62
%	0.02	0.37	2.40	24.24	72.95	87.57	12.43
%	0.03	0.48	5.03	32.11	62.33	81.84	18.16
%	0.04	0.82	8.42	38.80	51.90	75.94	24.06
%	0.23	3.34	18.74	45.19	32.47	63.07	36.94
%	0.84	9.52	30.53	41.90	17.19	49.71	50.30

equilibrium position. Two kinds of deformations were used: one-dimensional compression and simple shear at constant volume (see Fig. 8). During compression, one of the dimensions of the simulation box was reduced by a constant displacement step (whose value will be discussed later) while the positions of the atoms were rescaled in a homogeneous way. The other two perpendicular box sizes were not changed, therefore perpendicular stresses appeared and the compression test corresponded to a triaxial test. After the box displacement, a new equilibrium position was searched using the same Polak–Ribiere conjugate gradient algorithm as for the preparation. The shear deformation was done similarly by tilting the simulation box. The above deformations were repeated until the total cumulated strain reached 1%. This kind of applied deformation corresponds to a quasi-static low-frequency loading where the time elapsed between successive steps is supposed to be larger than the time needed to dissipate the energy [84]. We note, that ϵ is the normal strain applied during compression, and γ is the engineering shear strain applied upon simple shear tests.

The elementary strain steps were chosen to allow the system to respond elastically. In order to find the largest strain step allowed, the

following test was used: the box was deformed, relaxed and re-deformed to its original shape, then the displacement of the atoms were calculated between the original and the new configuration. The remaining displacements were divided by the box length to achieve strain-like unit. The histogram of the remaining displacements were then fitted by a log-normal distribution function. In Fig. 9 the position of the histogram peak is plotted as a function of the strain step size ($\delta\gamma$) for shear deformation. Until $\delta\gamma = 10^{-4}$ the average deformation stays elastic, but for larger steps the remaining displacements increase drastically and enter the plastic regime. Therefore the largest elementary strain step used was set to 10^{-4} which is consistent with previous measurements [30,35].

The stiffness tensor was then calculated both globally (at the scale of the system size), and locally (at a smaller coarse-graining scale). In order to identify the scale where the material loses eventually its local anisotropic components and becomes isotropic, the complete stiffness tensor was considered [7]. Another aim was to compare the numerically obtained constitutive laws to the experimental one, and to ascribe a microscopic interpretation to the measured elastic moduli, for different cumulative strain increments.

3.2. Global elastic properties

In order to measure the 21 elastic moduli [85] characterizing the macroscopic mechanical response, all systems were submitted to 6 different deformations: three one directional compressions along three different perpendicular axes and three simple shears along three perpendicular planes. The schematic description of the two major loading cases is shown in Fig. 8. The stress–strain relations show small fluctuations that are due to local irreversible events, also referred to as micro-plastic events [86–88,84,89,30]. In all cases the macroscopic deformation was calculated from the dimensions of the simulation

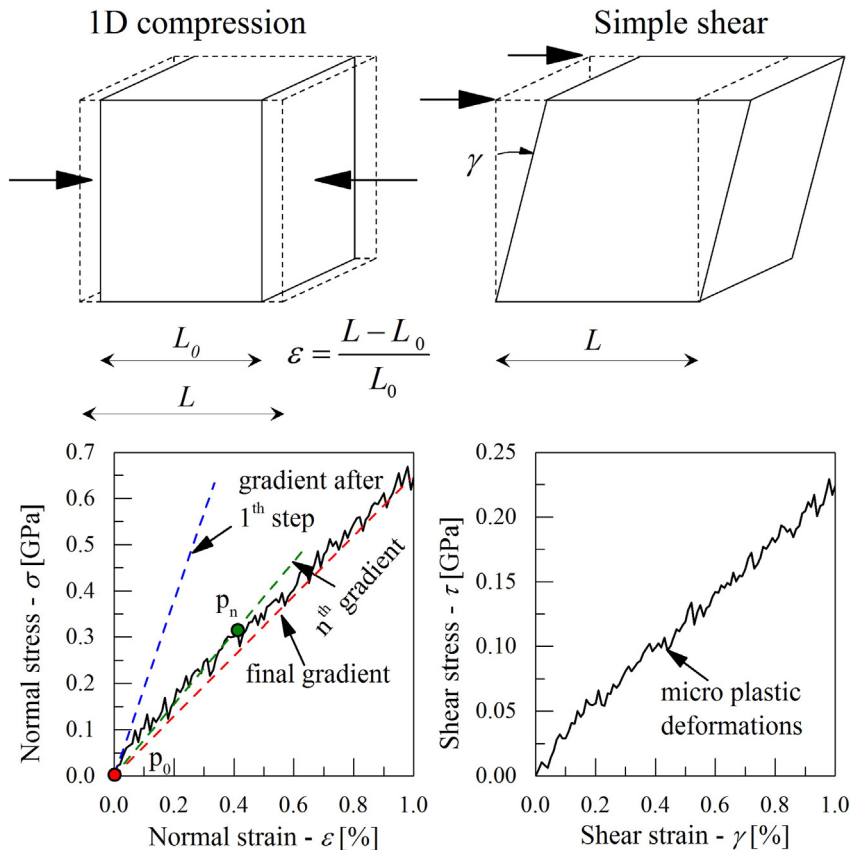


Fig. 8. Top: Two basic types of loading: triaxial compression (left), simple shear (right). Bottom: Early stages of the stress–strain relationships measured in the corresponding triaxial compression (left) and simple shear (right).

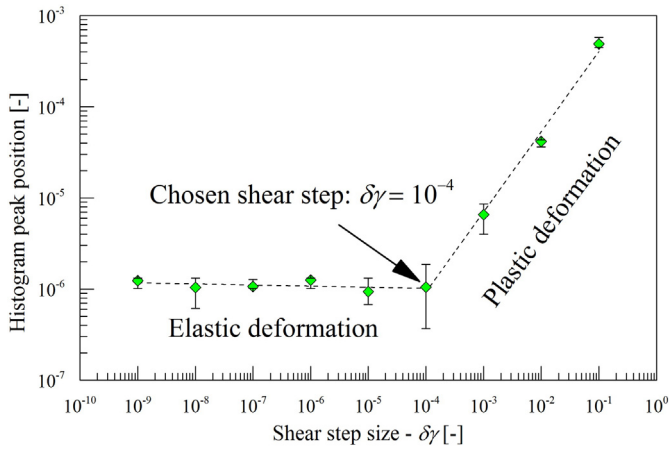


Fig. 9. Position of the peaks of the histograms of the displacement of the particles after a forth and back deformation step as a function of strain step size.

box. Stress was then measured by the summation of the per-atom stress values divided by the box volume. Voigt notation and engineering shear strains were used (Fig. 8) respectively. Hooke's law is then written as:

$$\boldsymbol{\sigma} = \mathbf{C}\boldsymbol{\epsilon}, \quad (6)$$

where \mathbf{C} is the stiffness matrix, $\boldsymbol{\sigma}$ and $\boldsymbol{\epsilon}$ are vector representations of the stress and strain tensor (Voigt notation). The applied strain ($\boldsymbol{\epsilon}$) is always calculated from the displacements between original p_0 and a deformed p_n state (e.g. see Fig. 8). $\boldsymbol{\epsilon}$ is the total strain separating two states, whatever the number of steps in-between. It will be referred to as the *global strain* or *applied strain* in the following. For example at 1% global strain (in other words with 1% strain resolution) we compute the material constants using the stress and strain increments between the initial configuration and one of the six different deformed configurations, which were compressed or sheared by a total cumulated amount of 1% (with the basic increment of 10^{-4} strain steps). Note that this deformation includes possible microplastic events and is not reversible at all scales. The stress is also calculated as the difference between the final and the initial value. The components of the stiffness matrix (\mathbf{C}) are calculated as a linear regression (n^{th} slope) between the first and the deformed configuration. Six different quasi-static deformation cases result in 36 equations. The stiffness matrix is symmetric. Therefore, a general, anisotropic material can be described by 21 unknowns. The six individual Eq. (6) were rewritten as an overdetermined equation system ($\|\mathbf{M}\mathbf{c} - \mathbf{s}\| = \min$) relating the tangent moduli to the stresses. The coefficient matrix (\mathbf{M} , size: 36×21) contains the strain values. The stiffness components are the unknowns (\mathbf{c} , size: 21×1), and the stress values are the constant terms (\mathbf{s} , size: 36×1). To solve the overdetermined system QR decomposition was used. Knowing that the equations are not fully independent, there is always 15 equations which are linear combination of the others. The relative error (Δ) is determined by substituting the stiffness components into the original equation system and then calculating the stress difference from the MD results.

In Fig. 10 the components of the stiffness tensor and Δ is plotted as a function of the applied global strain. The initial high value of the error indicates that the material deviates from linear elastic behavior especially for small strain steps, most probably due to the small plastic events. However, it is shown here that for the global measurements (unlike for the local measurements, as will be seen later), Δ is always smaller than 10%, which means that the error is small. In Fig. 11, the error (Δ) is plotted for different system sizes, at a global strain $\gamma = 0.5\%$ where the error was stabilized for all the sizes considered. It is shown here, that the size dependence of the relative error saturates when the system size becomes larger than $L = 50 \text{ \AA}$ (~ 9000 atoms).

This size can thus be considered as the minimum size needed to get reproducible macroscopic measurements of the elastic moduli. In the following, $L = 100 \text{ \AA}$ will be used.

In Fig. 10 one can see first that the green dashed group (from C_{14} to C_{56}), which represents the anisotropic components of the matrix is negligible compared to the other ones $C_{14} \approx 0.3 \text{ GPa}$). One can also see that the simulation box is large enough to recover the continuum isotropic and homogeneous description valid at large scales. Our system is indeed isotropic (with only two elastic constants) in the domain where the relative error is sufficiently small. Finally, 9 orthotropic material constants were calculated as a function of the applied strain: $E_x, E_y, E_z, G_{xy}, G_{xz}, G_{yz}, \nu_{zx}, \nu_{yx}$ and ν_{zy} [91]. They are shown in Fig. 12. For small applied strain, due to the large initial errors, some orthotropic stiffness components G_i are negative, which case violates Drucker's stability criterion [92]. These negative values correspond to local instabilities, or plastic events, occurring even at very small deformations which cannot simply be tracked experimentally, but changes the numerically computed precise value. In the same range of small strain increments ($\gamma < 0.1\%$), a large value of Δ indicates that linear elasticity is not valid at that scale. The maximum value for Δ is 10% and is reached at very low global strain (Fig. 10). For such a very small strain value, there is a strong variation of the elastic moduli. The same results hold for the potential of Pedone et al. [31]. Note that a better convergence criterion was found in Lennard-Jones like systems for the same system size [7]. At larger applied strain, the 9 orthotropic constants merge into 3 well defined elastic constants: a Young modulus E , a shear modulus G , and a related Poisson's ratio ν . The relative maximal difference between the orthotropic material constants is defined as:

$$\Delta C_i = \frac{(C_i^{\max} - C_i^{\min})}{\langle C_i \rangle}, \quad (7)$$

where C_i corresponds to E_i, G_i, ν_i . The maximum and the minimum are taken from three different components of the selected group. ΔC_i is used to characterize the orthotropy in the global elastic properties. As shown in Fig. 12(d), it decreases rapidly. Only a small fluctuation remains at large strains. It is thus possible to define the three elastic constants E, G and ν as the average between the three corresponding orthotropic values of each group, for each global strain. The difference between the measured average of the Poisson's ratio (ν) and the isotropically calculated one:

$$\nu_{ISO} = E/(2G) - 1, \quad (8)$$

quantifies the departure from the isotropic behavior. As shown in Fig. 13, the ratio between ν and ν_{ISO} goes to one, exponentially, with a characteristic applied strain (γ_c). This means that the isotropic behavior is indeed recovered after a global strain $\gamma_c = 0.16\%$. The bulk modulus K can be deduced from two orthotropic constants. It is shown in Fig. 12(e), that the best definition for K is obtained using the shear modulus and the Poisson's ratio, and is fluctuating when using the Young's modulus and the shear modulus. Indeed, the bulk modulus is not very well defined for slightly anisotropic materials, as it is the case here for small strains.

For small applied strain, the apparent materials stiffness observed in Fig. 10 and in Fig. 12, is always larger than in the later stages. This is a consequence of the accumulation of microplastic events for larger applied global strain. The apparent elastic moduli measured at large scale, and relatively large applied strains, are indeed the results of the succession of microplastic events not taken into account usually in small scale modeling [93,94]. A comparison between the experimental and the calculated isotropic material properties is shown in Fig. 14, as a function of Na_2O content. The simulated values were taken between 0.45% and 0.6% global strain by averaging the orthotropic constants. One can observe that the experimental values fit exceptionally well the simulated ones for compositions between 20% and 40% Na_2O . This

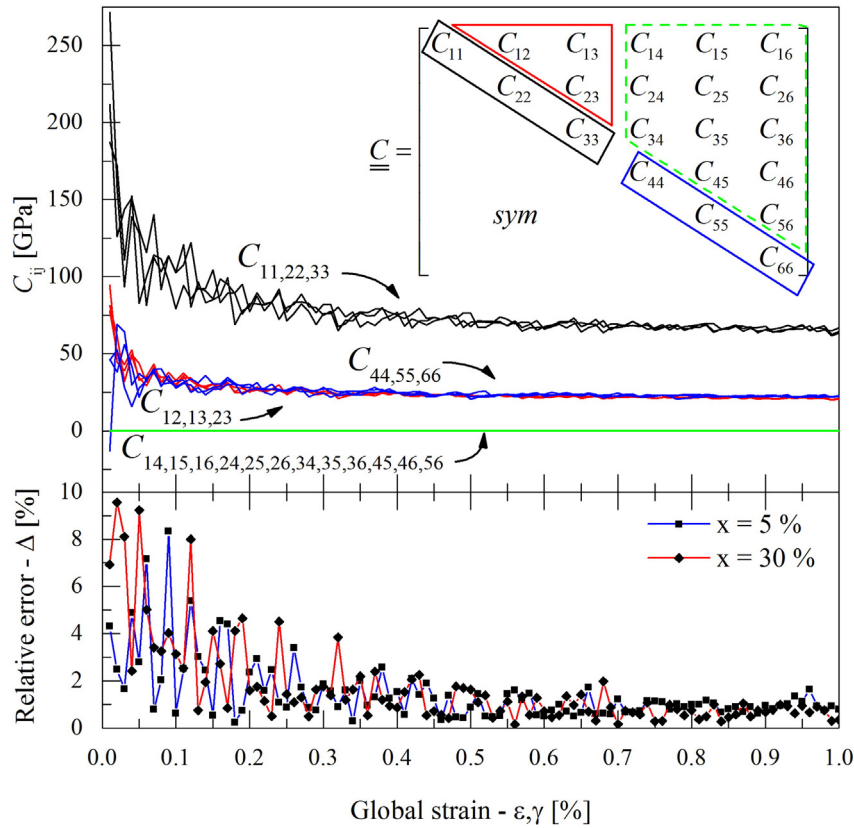


Fig. 10. Stiffness matrix components (for $x = 30\%$ mol Na_2O with the system size of 100 Å) and relative error (Δ) for two compositions ($x = 5\%$ mol Na_2O and $x = 30\%$ mol Na_2O), as a function of the global strain difference ϵ for compression and γ for shear.

is the range which is called stress-free (from 18% mol [95]) in sodium silicates. At this composition the sodium starts to act as network modifier and lowers the glass transition temperature. Fig. 14 shows that Young's and shear moduli change monotonously with the sodium content. The glass becomes stiffer when the amount of sodium decreases (despite the smaller interaction cutoff). The evolution of the Poisson's ratio and of the bulk modulus is a little more complicated (the Bulk modulus being computed with the help of the shear modulus and the Poisson's ratio as discussed before). In our simulations, in the stressed regime (low sodium content), we neglect the initial stress field present in the experimental samples. Therefore our samples appear more homogeneous and thus more rigid [96]. Note that this artificially enhanced rigidity for low sodium content was already mentioned in previous

studies on pure silica glasses [97,98]. The largest discrepancy appears in the bulk modulus.

As a conclusion, simulations replicate adequately the macroscopic elastic behavior of sodium silicate, but the experimental values of Young's and shear moduli are recovered only for sufficiently large applied strain ($\approx 0.4\%$) and sufficiently large sodium content. Our atomistic simulations suggest that the elastic moduli measured in glassy systems, within the experimental resolution, are only tangent moduli, and include a large number of microplastic events. This remark is important when looking for a rigorous microscopic definition of the elastic stiffness [93]. Moreover, the discrepancy between experimental and numerical values for low sodium content, suggests that additional parameters should be taken into account to increase the sources of heterogeneities in low sodium content samples [95,96,97]. We will now compare the global values of the elastic moduli to the local description of the elastic heterogeneities in our samples.

3.3. Local elastic properties

The local elastic properties of the materials can be derived in the same way as the global stiffness matrix. Local stress and strain fields are computed using a physically derived coarse-graining procedure proposed by Goldhirsch et al. [99]. It is based on the coarse-grained description of the density (Eq. (5)) combined with the mass conservation equation and with the momentum transport equation [99]. This method thus allows the preservation of the fundamental equations at all scales, with a proper definition of local strain and stress tensors. The coarse-graining procedure was done on a $100 \times 100 \times 100$ grid to calculate local stress and strain values, following a method analog to that used in the global case. To calculate the stiffness matrix 36 equations can be expressed for all grid points. Results are presented for 0.5% global strain deformation where the global moduli are already stable and reliable. The analysis focuses mainly on the composition of

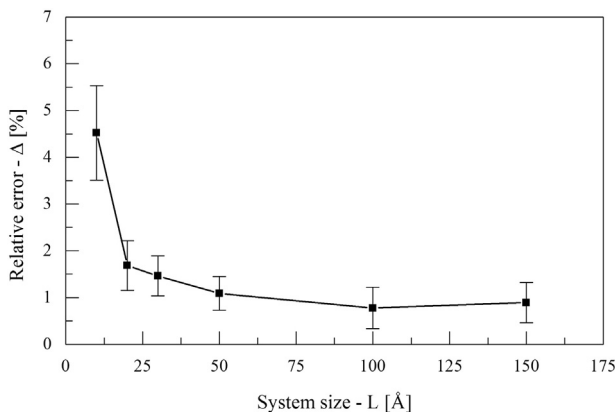


Fig. 11. Error function (Δ) for the global elastic moduli, as a function of the system size with $\gamma = 0.5\%$.

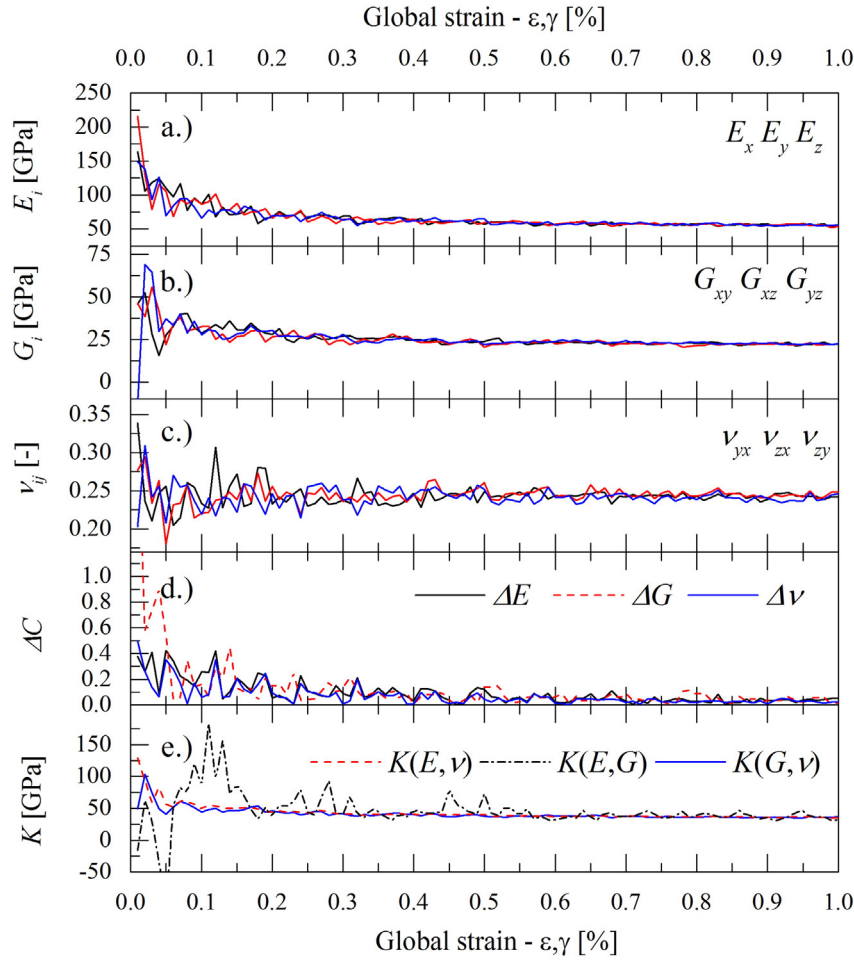


Fig. 12. a.–c.) Orthotropic material constants as a function of global strain. d.) Orthotropy for different material constant groups. e.) Calculated bulk modulus using the mean value of different orthotropic material constants (E, G, ν) [90].

30%mol Na_2O because it fits very well the experimental results, and thus gives us a reliable insight. Some comparison is made as well with the 5% Na_2O sample.

The coarse-graining scale (w in Eq. (5)) corresponds to the width of the Gaussian weight function, namely the area over which data are averaged. If w is taken too small, local equations for the stress may become singular. On the other hand for too large w , we get back the global behavior and loose information about the spatial heterogeneities.

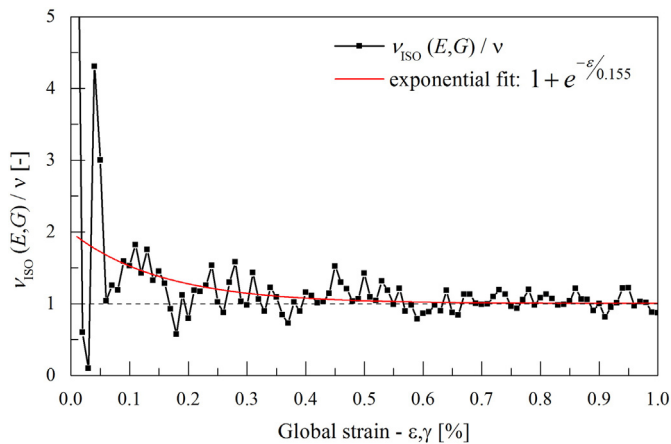


Fig. 13. Comparison of the Poisson's ratio ν obtained from the numerical measurement of E and G , with the Poisson's ratio ν_{ISO} obtained assuming isotropic elasticity.

The smallest reliable value for w , corresponds to a sufficiently small relative error Δ . In Fig. 15 the relative error Δ is shown as a function of the coarse-graining scale. The relative error decreases by increasing the coarse-graining scale. The initial stage can be well fitted with a power function, with initial values starting far above 10%. Tsamados et al. [7] found similar behavior for 2D Lennard-Jones glasses. The error is completely independent of w as soon w is sufficiently large to recover the macroscopic scale. The average relative error reduces below 3% at $w = 8 \text{ \AA}$ for $x = 30\%$ and $x = 5\%$ as well. For such a scale w , the maximum condition number of M was checked (not shown here), and a value smaller than 2 was found. Therefore, the solution and the results were considered reliable. At smaller scales where the errors are very large, a complete mechanical analysis would need more elaborated mechanical descriptions (like non-linear theories, or higher order gradient expansions [100]), but whose possible relevancy is beyond the scope of the present paper. We will thus consider in the following $w = 8 \text{ \AA}$ as a reliable choice for w .

In Fig. 16, the isotropic material constants are shown as a function of w . The results confirm the previous observations, namely, the fluctuations decrease as the coarse-graining scale increases. Around $w = 8 \text{ \AA}$ the local properties reach the global values within 5% precision for all compositions. As a result we definitely consider $w = 8 \text{ \AA}$ as the best coarse-graining scale for this analysis. Note that the convergence of the material constants to the macroscopic values depends on the sodium content (inset Fig. 16). Local elastic moduli are always stiffer than the global one for large sodium content ($x = 30\%$ mol), but softer for low sodium content ($x = 5\%$ mol). It is however not clear whether the convergence is faster or slower for the different compositions. For

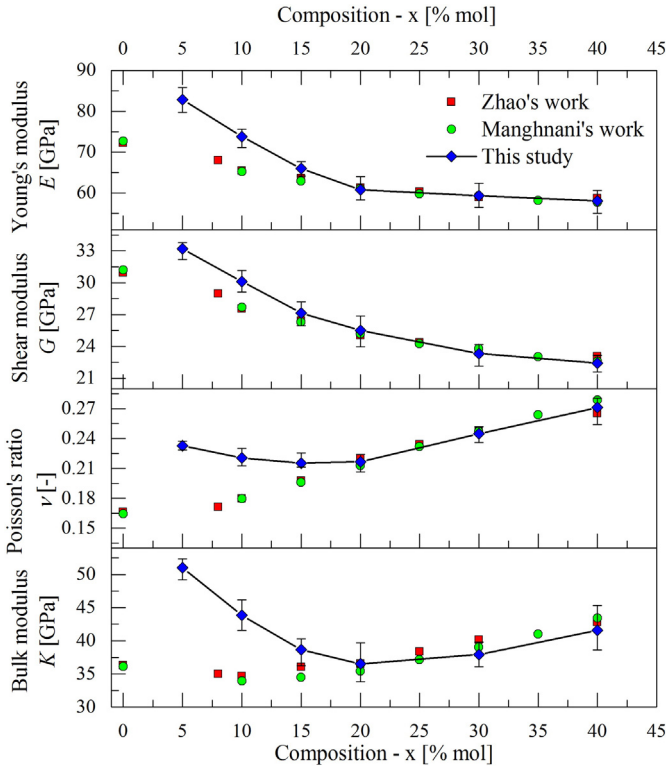


Fig. 14. Young's, shear, bulk moduli and Poisson's ratio as a function of composition (global strain = 0.45–0.6%). Comparison between simulated and experimental [69,70] values.

example, faster convergence of the Young's modulus (E) was observed with the material containing 30%mol than with 5%mol Na_2O content, but the opposite holds for the bulk modulus (K). Even if the silica network is less disturbed for smaller sodium contents, the local mechanical properties may converge in a slower manner. It means that the local variation of the composition could have stronger effects on the mechanical response for dilute sodium content. Similar results were observed also with experiments (see Fig. 14). The convergence from the local values of the elastic moduli to the global values is thus composition dependent.

We will now compare the local elastic moduli to the local chemical composition. The aim of this analysis is to infer a structural origin to

the composition sensitivity of elastic heterogeneities. In the following, a coarse-graining scale $w = 8 \text{ \AA}$ will be used for the calculation of local properties as discussed before.

Fig. 17 shows the local density maps of sodium and silicon, as well as the local shear and bulk moduli in the middle plane of the simulation box. The bulk modulus is computed from the local shear modulus and the local Poisson's ratio as discussed before. Correlations can be made visually between silicon density, bulk and shear moduli, while the local density of the sodium is anti-correlated with them. For quantitative comparison a correlation measurement is introduced:

$$\text{corr}(A, B) = \frac{\sum_m \sum_n (A_{nm} - \bar{A})(B_{nm} - \bar{B})}{\sqrt{\left(\sum_m \sum_n (A_{nm} - \bar{A})^2\right) \left(\sum_m \sum_n (B_{nm} - \bar{B})^2\right)}} \quad (9)$$

where A and B are two different quantities on the same n times m 2D grid. The \bar{A} stands for the mean value of the elements matrix A . The structural analysis in the previous section (especially Fig. 4) suggests that the correlation between silicon and oxygen should be high while the correlation between densities of sodium and silicon should be negative. Indeed we find: $\text{corr}(\text{Si}, \text{O}) = 0.972$ and $\text{corr}(\text{Si}, \text{Na}) = -0.882$. In Fig. 17(c) and (d) the contour maps of shear and bulk moduli are shown. The plots look slightly different but contain similar features indicating a medium correlation. In Tables 4 and 5 the correlation values between different moduli are shown for compositions of 5% and 30% sodium content respectively. The largest correlation was observed between the Young's and shear moduli. Bulk moduli are mainly correlated with Poisson's ratio, but also with shear moduli, especially for large sodium content. The bulk modulus is however not very well defined at small scale due to the lack of isotropy. This explains the large relative error bars in the correlation functions involving the bulk moduli. By looking at the density of atoms (Fig. 17(a) and (b)) correlations can be established between the elastic constants and different atomic species. The corresponding values are presented in Table 6. Silicon and oxygen have a strong positive correlation with Young's, shear and bulk moduli, while sodium has a negative correlation with all of them. Only a weak correlation is found between the local Poisson's ratio and the sodium density. Sodium weakens not only the shear modulus, as could be explained by a higher mobility of sodium ion due to weaker interactions with its neighbors (smaller effective charge), but it weakens also the Young's and bulk moduli. This proves that the materials rigidity is given by the silica network, and sodium weakens it locally by penetrating the system. The weakening of the original silica network by sodium explains easily the general decay of the global elastic moduli with sodium content (Fig. 14). The lack of isotropy at small scale makes however more difficult the connection between local and global bulk modulus. In agreement with experimental data, the numerically computed global bulk modulus increases with sodium content for large sodium content in opposition with the locally measured weakening. This may be due to the precise interconnection of the percolating cluster of sodium within the silica network that embed the global collapse of the structure, and consequently volume changes.

We have seen in this part, that the stiffness of sodium silicate is given by the silicon-oxygen network, which is weakened in general both microscopically and macroscopically by the presence of sodium ions. Global elastic moduli are recovered as the large scale convergence of coarse-grained local elastic moduli. The convergence scale depends on the composition, as well as on the modulus considered. For example, the convergence scale of the shear modulus is smaller for larger sodium content, but it is the opposite for the bulk modulus. The weakening of the elastic moduli by the presence of sodium ions does not apply for the bulk modulus with large sodium content, suggesting a specific sensitivity of pressure to sodium ions, probably due to large-scale connections in the channel-like structure discussed in Section 2.4. The

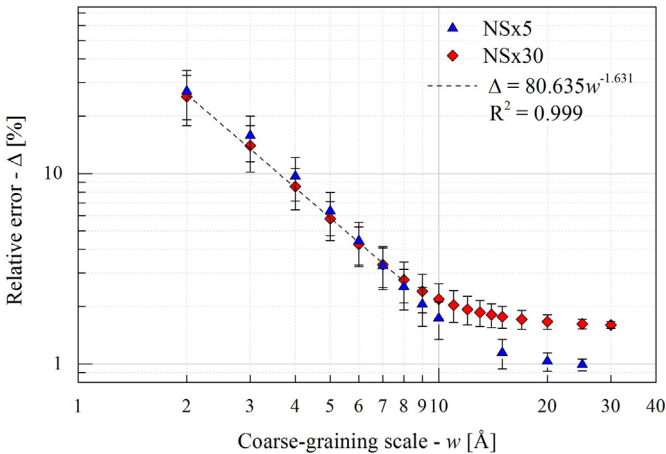


Fig. 15. Relative error of local estimations of the elastic moduli, as a function of the coarse-graining scale w (for $x = 30\%$ mol and $x = 5\%$ mol Na_2O , global strain = 0.5%).

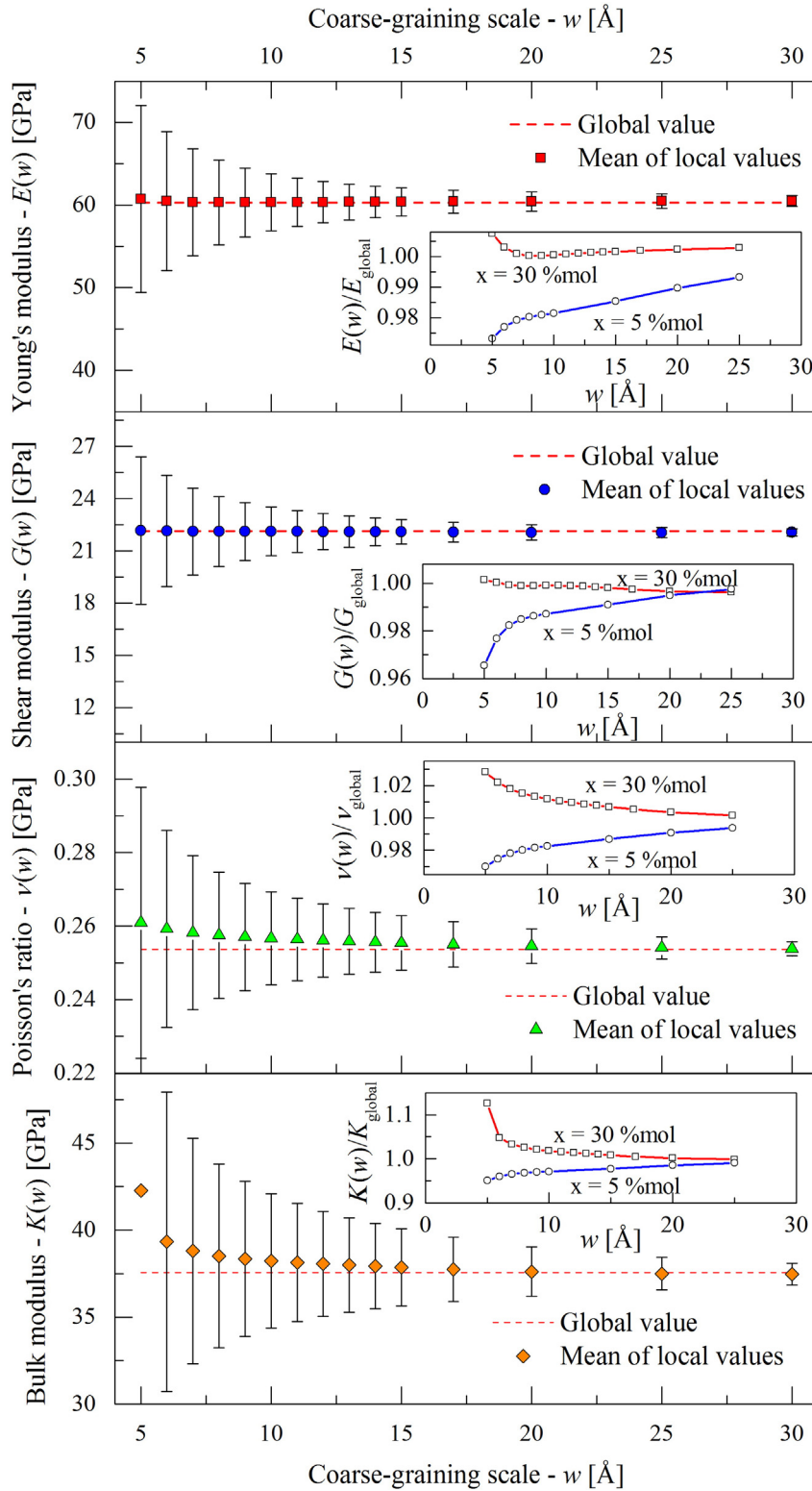


Fig. 16. Local Young's, shear, bulk moduli and Poisson's ratios as a function of the coarse-graining scale w (global strain = 0.5%). The investigated composition is $x = 30\%$ mol Na_2O . Insets: relative local moduli for two compositions $x = 5\%$ mol and 30% mol, as a function of w .

large scale description of the bulk moduli for large sodium content needs indeed a better understanding of the effect of large scale spatial correlations between sodium density and silica network on its elastic properties. This is beyond the scope of the present paper, that focuses on the numerical measurement of the role of sodium on the apparent linear elastic response.

4. Discussion

The present paper is a detailed numerical study of the early stages of the mechanical response of sodium-silicate glasses as a function of sodium content. We have shown three major results that are important to understand the microscopic origin of apparent elastic moduli: the first

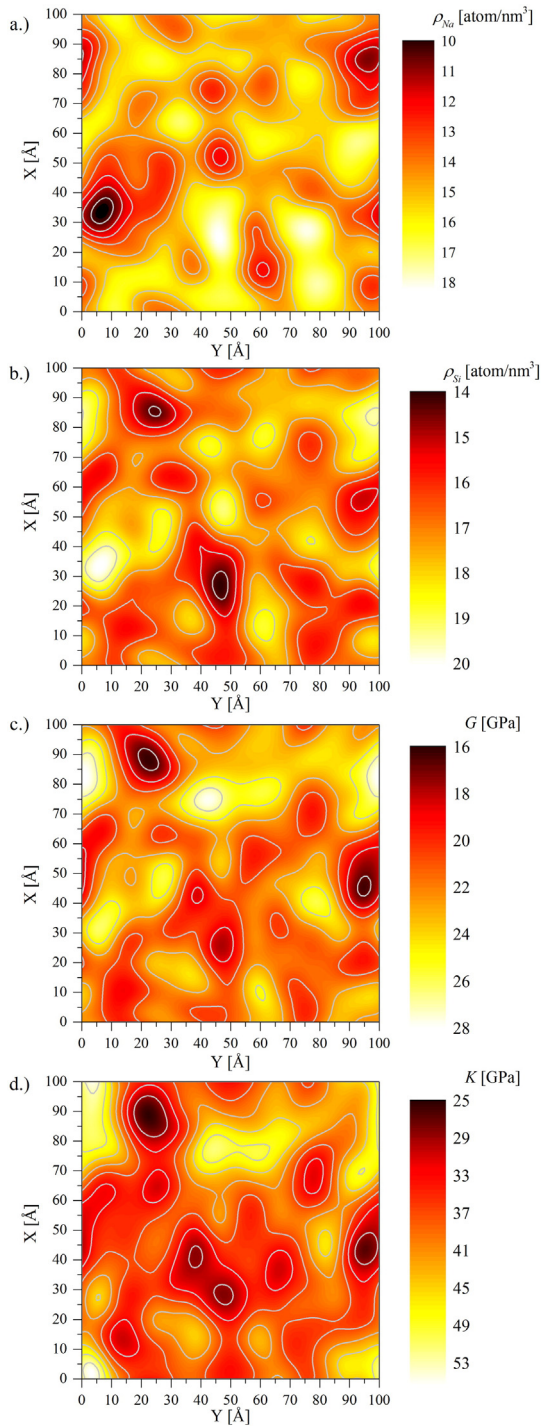


Fig. 17. (a) Sodium density map, (b) silicon density map, (c) local shear modulus map, (d) local bulk modulus map, for $x = 30\%$ mol Na_2O (global strain = 0.5%).

result concerns the description of empirical interactions and the role of the interaction cutoff on the mechanical properties; the second result is related to the existence of underlying microplastic events even at low

Table 4

Correlation between elastic constants, for sodium silicate containing $x = 5\%$ mol Na_2O .

$\text{corr}(A,B)$	E	G	K	ν
E	1	0.79 ± 0.06	0.51 ± 0.06	0.04 ± 0.05
G		1	0.72 ± 0.01	0.16 ± 0.09
K			1	0.79 ± 0.05
ν				1

Table 5

Correlation between elastic constants, for sodium silicate containing $x = 30\%$ mol Na_2O .

$\text{corr}(A,B)$	E	G	K	ν
E	1	0.86 ± 0.05	0.56 ± 0.07	-0.13 ± 0.08
G		1	0.77 ± 0.07	0.03 ± 0.18
K			1	0.65 ± 0.09
ν				1

applied strain; the third result is related to the convergence of local elastic properties and its sensitivity to the glass composition.

The influence of interaction cutoff on the mechanical properties of glasses was extensively studied before [12,62–64]. We see here that varying the cutoff of the non-Coulombic part of the interactions only is sufficient to affect strongly the pressure/density relation, and the elastic moduli. The cutoff value chosen to satisfy the pressure/density relation seems to be convenient as well for the elastic properties, and does not change sensibly the structural properties that compare quite well to the experiments. To match the glass densities measured in experiments, a moderate value for the cutoff is needed. It means that the cutoff is not just an approximation used to simplify the interactions, but is needed to describe more accurately intrinsic properties of glasses. The cutoff is shown to increase with the sodium content. A wrong estimate of the cutoff would lead to underestimation of the elastic moduli for low sodium content (a smaller cutoff inducing smaller stiffness). It was shown in opposite, that the numerical measurement obtained in this paper, gives rise to slightly larger estimates of the elastic moduli, especially for low sodium content. The cutoff is thus not responsible for this discrepancy. In general, the good comparison obtained between the numerical results and the experimental measurements strengthen strongly our method.

It is important to know how to define elastic moduli from a microscopic point of view, at least for materials design [101]. We have seen that the minimum size needed to recover size independent moduli is 50 Å for sodium-silicate glasses. Moreover, the elastic moduli are sensitive to the applied strain. For low applied strain ($\gamma < 0.1\%$), the elastic moduli measured in a 100 Å large sample fluctuate a lot. The material becomes isotropic at $\gamma = 0.16\%$, and then the two remaining elastic moduli saturate to a well defined value. It is thus somehow nonsense to identify the elastic moduli with an applied strain smaller than 0.16%. But for larger applied strains, the tangent moduli are properly defined. However, for such a large applied strain ($\gamma > 0.16\%$), elastic moduli do not correspond to strictly irreversible processes at small scales. Indeed, due to the large number of degrees of freedom at small scale (proportional to the number of atoms), it is highly probable that some dissipative events, or mechanical instabilities, occur during the deformation. It is indeed what happens in our numerical systems. This explains the apparent smaller stiffness observed at larger applied strains. These small scale dissipative processes, or microplastic events, were already invoked to explain the so-called “elastic anomaly” in silica glasses [30]. They were also observed with Brillouin scattering experiments in silica glasses, where the apparent decay of the sound velocity coincided with an increase in the linewidth used to quantify internal friction [8]. Our numerical measurements show that it is hopeless to define elastic moduli at a microscopic scale [93], without taking into account small scale dissipative processes. However, a realistic description of small scale dissipative processes involves sufficiently large

Table 6

Correlation between elastic constants and atomic species, for sodium silicate containing $x = 30\%$ mol Na_2O .

$\text{corr}(A,B)$	E	G	K	ν
Si	0.85 ± 0.06	0.86 ± 0.04	0.58 ± 0.10	-0.10 ± 0.17
O	0.90 ± 0.04	0.89 ± 0.04	0.64 ± 0.09	-0.03 ± 0.16
Na	-0.64 ± 0.10	-0.68 ± 0.05	-0.38 ± 0.12	0.21 ± 0.17

system sizes. This result is important, since the estimated elastic moduli can vary by a factor larger than three with the two different approaches. Moreover, such an approach definitely changes the perspectives of materials design.

Finally, the connection between local composition and local elastic moduli is very interesting to explore. Sodium-silicate glasses are example of materials where the increase of complexity in the composition simplify the mechanical response. Indeed, the presence of sodium ions always weakens the local stiffness. Low local stiffness is frequently considered as places where plastic instability will occur [7,102]. Sodium ions will thus probably act as catalysts for plastic deformation. Any process preventing sodium motion will increase the elastic limit. In opposite, adding sodium in the silica network should facilitate the plastic deformation and increase the ductility in a simple way. It would be interesting to pursue the comparison with the different failure modes observed in silicate materials [5]. At large scale, the complex organization of sodium ions along percolating prolate clusters affects the bulk modulus, therefore the description of the stiffness will probably become more complex during the plastic response upon hydrostatic compression. Such a work opens new perspectives in the study of plastic deformation.

5. Conclusion

To conclude, we have studied extensively the influence of the sodium content on the apparent elastic properties of a numerical model of sodium-silicate glass. We have first shown the influence of the cutoff of the non-Coulombic part of the interactions, on the elastic and structural properties of the glass. We have studied in detail the structural organization of Na ions in the silica network, showing evidence of percolating Na rich elongated clusters, with aspect ratio of 7–9. This long-range organization of sodium along percolating clusters, probably affects the large scale mechanical properties, especially the bulk modulus. It would be important now to understand the connection between the large scale organization of sodium with the bulk modulus, especially for low sodium content were channels yield to very heterogeneous structures. This question is important as well to understand, if the discrepancy observed in the bulk modulus for low sodium content results from channel-like structure, or from quenched stresses (as suggested previously).

The study of the early stages of the mechanical response upon triaxial compression, and simple shear, shows clearly the influence of the applied strain on the apparent elastic moduli. We concluded that below 0.1% strain, the elastic moduli measured from the stress-strain relation strongly fluctuate, due to intermittent instabilities. The regular and isotropic behavior is recovered at 0.16% strain. For such an applied strain, the material appears softer, due to the occurrence of microplastic events, as already shown in other systems. This observation raises the question of the proper definition of elastic moduli at a micro-scale. We suggest that the definition yielding to the best experimental comparison, includes the occurrence of microplastic events not detectable experimentally.

The study of local mechanical response has shown a progressive convergence from the local behavior to global properties, with increasing coarse-graining scale. This convergence depends on the composition, and on the modulus. For example, the convergence to the macroscopic value of the bulk modulus is slower for larger sodium content, but the convergence to the shear modulus is faster in the same case. At a local level, there is a strong correlation between silica network and higher stiffness, and opposite correlation with Na rich places. Sodium always weakens the local elastic properties, and should probably enhance the plastic instabilities. The smallest scale at which the material can be described within linear elasticity is $w = 8 \text{ \AA}$. Below that scale, displacements strongly vary, giving rise to ill-defined strain-tensor and non-linear relation between local stresses and local strains. The departure from the linear elastic behavior is however crucial

to induce irreversible motion. A predictive model of damage should thus take into account the processes occurring at such a small length-scale.

Acknowledgment

The authors thank M. Fábíán for sharing the experimental data, B. Ruta and D. Rodney for interesting discussions, as well as E. Barthel, B. Champagnon, C. Martinet and A. Mermet for stimulating our work. This work was supported by the French Research National Agency program MultiSil (ANR-13-BS09-0012). The authors wish to thank C. Yukna for his help in proofreading.

References

- [1] J.J. Thomas, H.M. Jennings, J.J. Chen, Influence of nucleation seeding on the hydration mechanisms of tricalcium silicate and cement, *J. Phys. Chem. C* 113 (11) (2009) 4327–4334.
- [2] N.N. Greenwood, A. Earnshaw, *Chemistry of the Elements*, Butterworth-Heinemann, Second edition, 1997.
- [3] J. Larosa-Thompson, P. Gill, B.E. Scheetz, M.R. Silsbee, Sodium silicate applications for cement and concrete, *Proceedings 10th ICCI1997* (3iii024).
- [4] C. Schittich, *Glass Construction Manual*, Birkhäuser Architecture, 2007.
- [5] T.M. Gross, M. Tomozawa, Fictive temperature-independent density and minimum indentation size effect in calcium aluminosilicate glass, *J. Appl. Phys.* 104 (6) (2008) 1–11.
- [6] R. Christensen, *Theory of Materials Failure*, Oxford University Press, 2013.
- [7] M. Tsamados, A. Tanguy, C. Goldenberg, J.L. Barrat, Local elasticity map and plasticity in a model Lennard-Jones glass, *Phys. Rev. E* 80 (2009) 026112.
- [8] D. Tielburger, R. Merz, R. Ehrenfels, S. Hunklinger, Thermally activated relaxation processes in vitreous silica: an investigation by Brillouin scattering at high pressures, *Phys. Rev. B* 45 (1992) 2750–2760.
- [9] W.-J. Drugan, J.-R. Willis, A micromechanics-based nonlocal constitutive equation and estimates of representative volume element size for elastic composites, *J. Mech. Phys. Solids* 44 (4) (1996) 497–524.
- [10] T. Kanit, S. Forest, I. Galliet, V. Mounoury, D. Jeulin, Determination of the size of the representative volume element for random composites: statistical and numerical approach, *Int. J. Solids Struct.* 40 (1314) (2003) 3647–3679.
- [11] D. Łydźba, A. Różański, Microstructure measures and the minimum size of a representative volume element: 2D numerical study, *Acta Geophys.* 62 (5) (2014) 10601086.
- [12] K. Vollmayr, W. Kob, K. Binder, Cooling-rate effects in amorphous silica: a computer-simulation study, *Phys. Rev. B* 54 (22) (1996) 15808–15827.
- [13] J. Horbach, W. Kob, Structure and dynamics of sodium disilicate, *Phil. Mag. B* 79 (11–12) (1999) 1981–1986.
- [14] A.N. Cormack, C. Yuan, Molecular dynamics simulation of silicate glasses, *Mol. Eng.* 6 (1–2) (1996) 183–227.
- [15] A.N. Cormack, X. Yuan, B. Park, Molecular dynamics simulations of silicate glasses and melts, *Glas. Phys. Chem.* 27 (1) (2001) 28–36.
- [16] X. Yuan, A.N. Cormack, Local structures of MD-modeled vitreous silica and sodium silicate glasses, *J. Non-Cryst. Solids* 283 (13) (2001) 69–87.
- [17] A.N. Cormack, J. Du, T.R. Zeitler, Sodium ion migration mechanisms in silicate glasses probed by molecular dynamics simulations, *J. Non-Cryst. Solids* 323 (2003) 147–154.
- [18] X. Yuan, A.N. Cormack, SiOSi bond angle and torsion angle distribution in vitreous silica and sodium silicate glasses, *J. Non-Cryst. Solids* 319 (12) (2003) 31–43.
- [19] J. Du, A.N. Cormack, The medium range structure of sodium silicate glasses: a molecular dynamics simulation, *J. Non-Cryst. Solids* 349 (2004) 66–79.
- [20] A. Meyer, J. Horbach, W. Kob, F. Kargl, H. Schober, Channel formation and intermediate range order in sodium silicate melts and glasses, *Phys. Rev. Lett.* 93 (2) (2004) 027801.
- [21] A. Tilocca, N.H. de Leeuw, A.N. Cormack, Shell-model molecular dynamics calculations of modified silicate glasses, *Phys. Rev. B* 73 (2006) 104209.
- [22] S. Ispas, T. Charpentier, F. Mauri, D.R. Neuville, Structural properties of lithium and sodium tetrasilicate glasses: molecular dynamics simulations versus NMR experimental and first-principles data, *Solid State Sci.* 12 (2) (2010) 183–192.
- [23] L. Adkins, A. Cormack, Large-scale simulations of sodium silicate glasses, *J. Non-Cryst. Solids* 357 (14) (2011) 2538–2541.
- [24] K. Muralidharan, J.H. Simmons, P.A. Deymier, K. Runge, Molecular dynamics studies of brittle fracture in vitreous silica: review and recent progress, *J. Non-Cryst. Solids* 351 (18) (2005) 1532–1542.
- [25] F. Léonforte, A. Tanguy, J. Wittmer, J.L. Barrat, Inhomogeneous elastic response of silica glass, *Phys. Rev. Lett.* 97 (5) (2006) 055501.
- [26] C.L. Rountree, S. Prades, D. Bonamy, E. Bouchaud, R. Kalia, C. Guillot, A unified study of crack propagation in amorphous silica: using experiments and simulations, *J. Alloys Compd.* 434–435 (2007) 60–63.
- [27] A. Pedone, G. Malavasi, M.C. Menziani, U. Segre, A.N. Cormack, Molecular dynamics studies of stress-strain behavior of silica glass under a tensile load, *Chem. Mater.* 20 (13) (2008) 4356–4366.
- [28] A. Pedone, G. Malavasi, M.C. Menziani, U. Segre, A.N. Cormack, Role of magnesium in soda-lime glasses: insight into structural, transport, and mechanical properties through computer simulations, *J. Phys. Chem. C* 112 (2008) 11034–11041.

- [29] C.L. Rountree, D. Vandembroucq, M. Talamali, E. Bouchaud, S. Roux, Plasticity-induced structural anisotropy of silica glass, *Phys. Rev. Lett.* 102 (2009) 195501.
- [30] B. Mantisi, A. Tanguy, G. Kermouche, E. Barthel, Atomistic response of a model silica glass under shear and pressure, *Eur. Phys. J. B* 85 (9) (2012) 1–14.
- [31] A. Pedone, G. Malavasi, M.C. Menziani, A.N. Cormack, U. Segre, A new self-consistent empirical interatomic potential model for oxides, silicates, and silica-based glasses, *J. Phys. Chem. B* 110 (24) (2006) 11780–11795.
- [32] A. Takada, Molecular dynamics simulation of deformation in SiO₂ and Na₂O–SiO₂ glasses, *J. Ceram. Soc. Jpn.* 116 (1356) (2008) 880–884.
- [33] A. Tanguy, J.-P. Wittmer, F. Léonforte, J.-L. Barrat, Continuum limit of amorphous elastic bodies: a finite-size study of low-frequency harmonic vibrations, *Phys. Rev. B* 66 (2002) 174205.
- [34] F. Léonforte, A. Tanguy, J.P. Wittmer, J.-L. Barrat, Continuum limit of amorphous elastic bodies II: linear response to a point source force, *Phys. Rev. B* 70 (2004) 014203.
- [35] F. Léonforte, R. Boissière, A. Tanguy, J. Wittmer, J.L. Barrat, Continuum limit of amorphous elastic bodies. III. three-dimensional systems, *Phys. Rev. B* 72 (2005) 224206.
- [36] A. Tanguy, Vibration modes and characteristic length scales in amorphous materials, *JOM* 67 (8) (2015) 1832–1839.
- [37] D. Rodney, A. Tanguy, D. Vandembroucq, Modeling the mechanics of amorphous solids at different length scale and time scale, *Model. Simul. Mater. Sci. Eng.* 19 (8) (2011) 083001.
- [38] C. Goldenberg, A. Tanguy, J.-L. Barrat, Particle displacements in the elastic deformation of amorphous materials: Local fluctuations vs. non-affine field, *Europhys. Lett.* 80 (1) (2007) 16003.
- [39] N. Zotov, H. Keppeler, The structure of sodium tetrasilicate glass from neutron diffraction, reverse Monte Carlo simulations and Raman spectroscopy, *Phys. Chem. Miner.* 25 (4) (1998) 259–267.
- [40] C. Karlsson, E. Zanghellini, J. Swenson, B. Roling, D. Bowron, L. Börjesson, Structure of mixed alkali/alkaline-earth silicate glasses from neutron diffraction and vibrational spectroscopy, *Phys. Rev. B* 72 (2005) 064206.
- [41] M. Fábian, P. Jávári, E. Sváb, G. Mészáros, T. Proffén, E. Veress, Network structure of 0.7SiO₂–0.3Na₂O glass from neutron and X-ray diffraction and rmc modelling, *J. Phys. Condens. Matter* 19 (33) (2007) 335209.
- [42] L. Cormier, G. Calas, B. Beuneu, Structural changes between soda-lime silicate glass and melt, *J. Non-Cryst. Solids* 357 (3) (2011) 926–931.
- [43] J.F. Emerson, P.E. Stallworth, P.J. Bray, High-field ²⁹Si NMR studies of alkali silicate glasses, *J. Non-Cryst. Solids* 113 (23) (1989) 253–259.
- [44] H. Maekawa, T. Maekawa, K. Kawamura, T. Yokokawa, The structural groups of alkali silicate glasses determined from ²⁹Si MAS-NMR, *J. Non-Cryst. Solids* 127 (1) (1991) 53–64.
- [45] T. Charpentier, S. Ispas, M. Profeta, F. Mauri, C.J. Pickard, First-principles calculation of ¹⁷O, ²⁹Si, and ²³Na NMR spectra of sodium silicate crystals and glasses, *J. Phys. Chem. B* 108 (13) (2004) 4147–4161.
- [46] M. Naji, D. De Sousa Meneses, G. Guimbretière, Y. Vaills, In situ high-temperature probing of the local order of a silicate glass and melt during structural relaxation, *J. Phys. Chem. C* 119 (16) (2015) 8838–8848, <http://dx.doi.org/10.1021/jp512234k>.
- [47] G. Kermouche, E. Barthel, D. Vandembroucq, P. Dubujet, Mechanical modelling of indentation-induced densification in amorphous silica, *Acta Mater.* 56 (13) (2008) 3222–3228.
- [48] R. Lacroix, G. Kermouche, J. Teisseire, E. Barthel, Plastic deformation and residual stresses in amorphous silica pillars under uniaxial loading, *Acta Mater.* 60 (15) (2012) 5555–5566.
- [49] V. Keryvin, J.-X. Meng, S. Gicquel, J.-P. Guin, L. Charleux, J.-C. Sangleboeuf, P. Pilvin, T. Rouxel, G.L. Quilliec, Constitutive modeling of the densification process in silica glass under hydrostatic compression, *Acta Mater.* 62 (2014) 250–257.
- [50] S. Plimpton, Fast parallel algorithms for short-range molecular dynamics, *J. Comput. Phys.* 117 (1995) 1–19.
- [51] H.J.C. Berendsen, J.P.M. Postma, W.F. van Gunsteren, A. DiNola, J.R. Haak, Molecular dynamics with coupling to an external bath, *J. Chem. Phys.* 81 (8) (1984) 3684–3690.
- [52] D. Frenkel, B. Smit, *Understanding Molecular Simulations*, Academic Press, London, 2002.
- [53] R. Vuilleumier, N. Sator, B. Guillot, Computer modeling of natural silicate melts: what can we learn from ab initio simulations, *Geochim. Cosmochim. Acta* 73 (20) (2009) 6313–6339.
- [54] J.A.N. Zasadzinski, A new heat transfer model to predict cooling rates for rapid freezing fixation, *J. Microsc.* 150 (2) (1988) 137–149.
- [55] K. Binder, W.W. Kob, *Glassy Materials and Disordered Solids: An Introduction to their Statistical Mechanics*, World Scientific, Singapore, 2005.
- [56] S. Tsuneyuki, Y. Matsui, H. Aoki, M. Tsukada, New pressure-induced structural transformations in silica obtained by computer simulation, *Nature* 339 (1989) 209–211.
- [57] B.W.H. van Beest, G.J. Kramer, R.A. van Santen, Force fields for silicas and aluminophosphates based on ab initio calculations, *Phys. Rev. Lett.* 64 (1990) 1955–1958.
- [58] A. Pedone, G. Malavasi, A.N. Cormack, U. Segre, M.C. Menziani, Insight into elastic properties of binary alkali silicate glasses; prediction and interpretation through atomistic simulation techniques, *Chem. Mater.* 19 (2007) 3144–3154.
- [59] Y. Guissani, B. Guillot, A numerical investigation of the liquid-vapor coexistence curve of silica, *J. Chem. Phys.* 104 (19) (1996) 7633–7644.
- [60] M. Rarivomanantsoa, P. Jund, R. Jullien, Sodium diffusion through amorphous silica surfaces: a molecular dynamics study, *J. Chem. Phys.* 120 (10) (2004) 4915–4920.
- [61] A. Kerrache, V. Teboul, A. Monteil, Screening dependence of the dynamical and structural properties of BKS silica, *Chem. Phys.* 321 (12) (2006) 69–74.
- [62] V. Teboul, S. Chausseidant, Cutoff effect in molecular dynamics simulations of interaction induced light scattering spectra, *Comput. Phys. Commun.* 105 (2–3) (1997) 151–158.
- [63] C. Huang, C. Li, P. Choi, K. Nandakumar, L. Kostjuk, Effect of cut-off distance used in molecular dynamics simulations on fluid properties, *Mol. Simul.* 36 (11) (2010) 856–864.
- [64] K. Dilrukshi, M. Dewapriya, U. Puswewala, Size dependence and potential field influence on deriving mechanical properties of carbon nanotubes using molecular dynamics, *Theor. Appl. Mech. Lett.* 5 (4) (2015) 167–172.
- [65] M.P. Allen, D.J. Tildesley, *Computer Simulation of Liquids*, Clarendon Press, 1987.
- [66] W. Smith, G.N. Greaves, M.J. Gillan, Computer simulation of sodium disilicate glass, *J. Chem. Phys.* 103 (1995) 3091–3097.
- [67] J.R. Kermode, S. Cereda, P. Tangney, A.D. Vita, A first principles based polarizable O(N) interatomic force field for bulk silica, *J. Chem. Phys.* 133 (9) (2010) 094102.
- [68] P. Debye, E. Hückel, The theory of electrolytes. I. Lowering of freezing point and related phenomena, *Phys. Z.* 24 (1923) 185–206.
- [69] M.H. Manghnani, B.K. Singh, Proceedings of Xth international congress on glass, japan ceramic society, kioto n111974 104.
- [70] Q. Zhao, M. Guerette, G. Scannell, L. Huang, In-situ high temperature Raman and Brillouin light scattering studies of sodium silicate glasses, *J. Non-Cryst. Solids* 358 (2012) 3418–3426.
- [71] G. Greaves, EXAFS and the structure of catalysts, *Catal. Today* 2 (5) (1985) 581–584.
- [72] P. Jund, W. Kob, R. Jullien, Channel diffusion of sodium in a silicate glass, *Phys. Rev. B* 64 (2001) 134303.
- [73] A.N. Cormack, J. Du, T.R. Zetler, Alkali ion migration mechanisms in silicate glasses probed by molecular dynamics simulations, *Phys. Chem. Chem. Phys.* 4 (2002) 3193–3197.
- [74] E. Sunyer, P. Jund, R. Jullien, Matrix-controlled channel diffusion of sodium in amorphous silica, *J. Phys. Condens. Matter* 15 (26) (2003) L431.
- [75] M. Pota, A. Pedone, G. Malavasi, C. Durante, M. Cocchi, M.C. Menziani, Molecular dynamics simulations of sodium silicate glasses: optimization and limits of the computational procedure, *Comput. Mater. Sci.* 47 (3) (2010) 739–751.
- [76] M. Bauchy, M. Micoulaut, From pockets to channels: density-controlled diffusion in sodium silicates, *Phys. Rev. B* 83 (2011) 184118.
- [77] B. Bollobás, O. Riordan, *Silicates*, Cambridge University Press, 2006.
- [78] Y.-B. Yi, A.M. Sastry, Analytical approximation of the two-dimensional percolation threshold for fields of overlapping ellipses, *Phys. Rev. E* 66 (2002) 066130.
- [79] E. Lakatos, I. Bojtár, Trabecular bone adaptation in a finite element frame model using load dependent fabric tensors, *Mech. Mater.* 44 (2012) 130–138.
- [80] S.L. Roux, V. Petkov, *ISAACS – interactive structure analysis of amorphous and crystalline systems*, *J. Appl. Crystallogr.* 43 (1) (2010) 181–185.
- [81] D. Theodorouand, U.W. Suter, Atomistic modeling of mechanical properties of polymeric glasses, *Macromolecules* 19 (1) (1986) 139–154.
- [82] D. Brown, J.H.R. Clarke, Molecular dynamics simulation of an amorphous polymer under tension. 1. Phenomenology, *Macromolecules* 24 (8) (1991) 2075–2082.
- [83] M. Parrinello, A. Rahman, Strain fluctuations and elastic constants, *J. Chem. Phys.* 76 (5) (1982) 2662–2666.
- [84] A. Tanguy, F. Léonforte, J.L. Barrat, Plastic response of a 2D Lennard-Jones amorphous solid: detailed analyses of the local rearrangements at very slow strain rate, *Eur. Phys. J. E* 20 (2006) 355–364.
- [85] G.A. Holzapfel, *Nonlinear Solid Mechanics*, Wiley, 2001.
- [86] F. Spaepen, A microscopic mechanism for steady state inhomogeneous flow in metallic glasses, *Acta Metall.* 25 (4) (1977) 407–415.
- [87] A.S. Argon, Plastic deformation in metallic glasses, *Acta Metall.* 27 (1) (1979) 47–58.
- [88] A. Lemaître, J.-L. Chaboche, *Mécanique Des matériaux Solides*, Dunod, 2004.
- [89] S. Karmakar, A. Lemaître, E. Lerner, I. Procaccia, Predicting plastic flow events in athermal shear-strained amorphous solids, *Phys. Rev. Lett.* 104 (2010) 215502.
- [90] A.C. Ugural, S.K. Fenster, *Advanced Strength and Applied Elasticity*, Elsevier Science Ltd., 1975.
- [91] L.P. Kollár, G.S. Springer, *Mechanics of Composite Structures*, Cambridge University Press, 2009.
- [92] D.C. Drucker, A definition of a stable inelastic material, *ASME J. Appl. Mech.* 26 (1959) 101–105.
- [93] S. Alexander, Amorphous solids: their structure, lattice dynamics and elasticity, *Phys. Rep.* 296 (1998) 65–236.
- [94] H. Mizuno, S. Mossa, J.-L. Barrat, Measuring spatial distribution of the local elastic modulus in glasses, *Phys. Rev. E* 87 (2013) 042306.
- [95] T. Qu, Non-aging and self-organization in network glasses (Ph.D. thesis) Division of Research and Advanced Studies of the University of Cincinnati, 2004.
- [96] W. Voigt, *Elementare Mechanik Als Einleitung in Das Studium Der Theoretischen Physik*, Veit and comp., Leipzig, 1889.
- [97] T.T. To, D. Bougeard, K.S. Smirnov, Molecular dynamics study of the vibrational pattern of ring structures in the Raman spectra of vitreous silica, *J. Raman Spectrosc.* 39 (12) (2008) 1869–1877.
- [98] N. Shchepanov, B. Mantisi, P. Umari, A. Tanguy, Detailed analysis of plastic shear in the Raman spectra of SiO₂ glass, *J. Non-Cryst. Solids* 428 (2015) 6–19.
- [99] I. Goldhirsch, C. Goldenberg, On the microscopic foundations of elasticity, *Eur. Phys. J. E* 9 (3) (2002) 245–251.
- [100] A.C. Eringen, *Nonlocal Continuum Field Theories*, Springer-Verlag, New York, 2002.
- [101] A.I. Salimon, M.F. Ashby, Y. Brechet, A.L. Greer, Bulk metallic glasses: what are they good for? *Mater. Sci. Eng. A* 375–377 (2004) 385–388.
- [102] M.L. Manning, A.J. Liu, Vibrational modes identify soft spots in a sheared disordered packing, *Phys. Rev. Lett.* 107 (2011) 108302.